

# Cavity optomechanical ultrasound sensing

Sahar Basiri-Esfahani<sup>1,2</sup>, Ardalan Armin<sup>1,2</sup>, Stefan Forstner<sup>1</sup>, and Warwick P. Bowen<sup>1a</sup>

<sup>1</sup>*ARC Centre for Engineered Quantum Systems,  
School of Mathematics and Physics, The University of Queensland,  
St Lucia, QLD 4072, Australia and*

<sup>2</sup>*Department of Physics, Swansea University, Singleton Park,  
Swansea SA2 8PP, Wales, United Kingdom*

## Abstract

Ultrasound sensors have wide applications across science and technology. However, improved sensitivity is required for both miniaturisation and increased spatial resolution. Here, we introduce cavity optomechanical ultrasound sensing, where dual optical and mechanical resonances enhance the ultrasound signal. We achieve noise equivalent pressures of 10–100  $\mu\text{Pa}/\sqrt{\text{Hz}}$  at tens-of-kilohertz to megahertz frequencies in a microscale silicon-chip-based sensor with  $>112$  dB dynamic range. This sensitivity is five orders-of-magnitude superior to similar sensors that use optical resonance alone and, normalised to sensing area, surpasses all previous ultrasound sensors by more than a thousand-fold. The noise floor is, for the first time, dominated by collisions from molecules in the gas within which the acoustic wave propagates. This new approach to acoustic sensing could find applications ranging from biomedical imaging and assays, to autonomous navigation, trace gas sensing, and scientific exploration of the life-induced-vibrations of single cells.

---

<sup>a</sup> w.bowen@uq.edu.au

Detection of acoustic waves is essential for many applications including medical imaging, sonar, navigation, trace gas sensing and industrial processes [1–3]. Most acoustic sensors transform an acoustic pressure wave into vibrations of a mechanical element, and detect these vibrations electrically via changes in piezoelectricity [4], resistivity [5], magnetic transduction or capacitance [6]. For many applications, high spatial, temporal and directional resolution is a key requirement [7, 8], with photoacoustic imaging being one notable example [9]. This has driven development towards both ultrasonic frequencies, with their correspondingly short acoustic wavelengths, and microscale sensing devices that are capable of resolving such waves at, or near, their diffraction limit [10]. The degradation in acoustic sensitivity that comes hand-in-hand with operation at higher frequencies and with smaller sensing areas presents a major challenge [11]. While, for an acoustic wave propagating through gas, the sensitivity is only fundamentally limited by the random momentum kicks from gas molecules as they collide with the sensor, all existing acoustic sensors are far from this limit. Their noise floor is, instead, typically dominated by electronic noise. This has motivated recent progress in photonic acoustic sensors [10, 13].

Over the past decade, cavity optomechanical sensors have emerged as a new class of ultraprecise photonic sensors [14–16]. These sensors integrate a high quality mechanical resonator with a high quality optical cavity (see e.g. [17, 18]). The mechanical resonator amplifies the mechanical vibrations introduced by resonant signals and provides isolation from environmental thermal noise, while the cavity resonantly enhances the optical response to the mechanical vibrations. A characteristic feature of cavity optomechanical sensors is that they are often only limited by optical shot noise and mechanical thermal noise, allowing the intrinsic limits in sensing performance to be approached [13]. This provides the ability to perform exquisitely sensitive optical measurements, with sub-attometre precision [20]. At kilometre scales it has proved crucial for the successful detection of gravitational waves [21]; while at micro- and nano-scales it has enabled high performance acceleration, magnetic field, and force sensors [22–25], as well as provided a new approach to control the quantum physics of massive objects, allowing quantum ground-state cooling [26–29] and the generation of macroscopic non-classical states of motion [30–32], with applications in future quantum technologies [33–36].

In this article we extend cavity optomechanical sensing to the measurement of acoustic and ultrasonic waves, using a lithographically fabricated device suspended above a silicon

chip via thin tethers [37]. By engineering its structure for high acoustic sensitivity, we reach the regime where gas molecule collisions dominate the noise floor. This allows noise equivalent pressures of 10–100  $\mu\text{Pa}/\sqrt{\text{Hz}}$  at a range of frequencies between 10 kHz and 1 MHz. Compared to acoustic sensors that use similar, but non-suspended, optical cavities and rely on refractive index shifts rather than nanomechanical motion [38, 39], this represents a more than five order-of-magnitude advance. Furthermore, normalised by device area, our sensor outperforms all previous acoustic sensors by more than three orders-of-magnitude at frequencies between 200 kHz and 1 MHz.

## RESULTS

### Working principles of cavity opto-mechanical acoustic sensing

In general, cavity optomechanical sensors consist of a mechanically compliant element coupled to an optical cavity. The mechanical element is displaced in response to an external stimulus – in our case an acoustic wave. The optical cavity resonantly enhances the optical response to this displacement, allowing precise measurement of the stimulus. Commonly, the coupling from displacement to optical response can occur in one of two ways: dispersive [40] or dissipative coupling [41, 42], both of which are used in our sensor. With dispersive coupling, the mechanical displacement alters the cavity length, and therefore optical resonance frequency (See Fig. 1a&b). In dissipative coupling, the displacement instead alters the cavity decay rate, by either altering the optical input coupling or intra-cavity loss (See Fig. 1d&e). The concept of ultrasound sensors based on each coupling mechanism is shown in Fig. 1, using a simple Fabry-Perot cavity as an illustrative example.

In the simple case where the mechanical element has a single mechanical resonance, the minimum detectable acoustic pressure for both dispersive and dissipative cavity optomechanical sensing is given by

$$P_{\min}(\omega) = \frac{1}{rA} \sqrt{2(\mu l + m\gamma)k_B T + \frac{1}{N|\chi(\omega)|^2}}, \quad (1)$$

where  $A$  and  $T$  are the area and temperature of the sensor, respectively, and we assume that the laser used to probe the optical response is shot noise limited (see Supplementary Information for calculation). The acoustic pressure wave will only exert a force if it induces

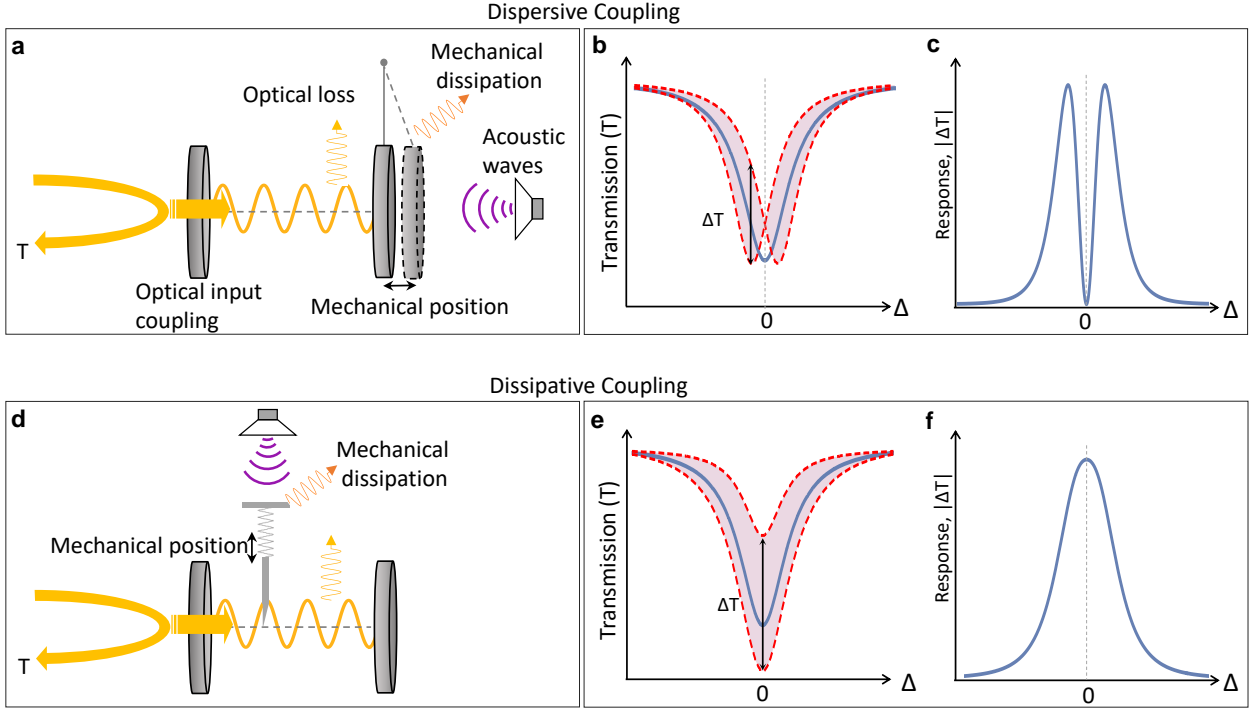


**FIG. 1. Principles of dispersive and dissipative cavity optomechanical acoustic sensing.** (a&d) Conceptual schematics of Fabry-Perot cavity-based dispersive (a) and dissipative (d) sensors. In (a) an applied acoustic force drives harmonic oscillation of a movable cavity end-mirror modulating the length and resonance frequency of the cavity. In (d) the force drives a mechanical element that modulates the decay rate of the cavity. The modulation is monitored via the change in optical transmission from the cavity. (b&e) Cavity transmission in the presence of dispersive and dissipative coupling, respectively. The solid blue curves show the cavity transmission for the initial position of the mechanical element while the red dashed curves show the modified cavity transmission due to displacement of the mechanical element. (c&f) Amplitude of external-force driven modulation in transmission of the cavity optomechanical system for dispersive and dissipative coupling, respectively, versus the detuning  $\Delta$  of the input laser field from the cavity resonance.

a pressure difference between the top and bottom surfaces of the mechanical element. This is quantified by  $r$ , the ratio of the pressure difference to the peak pressure at the antinode of the acoustic wave. The first of the three terms under the square-root quantifies the noise introduced by collisions with molecules in the gas surrounding the resonator, where  $\mu$  is the coefficient of viscosity of the gas and  $l$  is a device geometry-dependent characteristic length-

scale. The second term quantifies the thermal force noise introduced by the fluctuation-dissipation theorem due to the intrinsic damping of the mechanical resonator.  $m$  is the resonator effective mass which is generally close to but less than the actual mass, and  $\gamma$  is the intrinsic mechanical damping rate. The third term quantifies the optical measurement noise, with  $N$  being the number of photons in the cavity and  $\chi(\omega)$  an optomechanical susceptibility which is a function of acoustic drive frequency  $\omega$ . The functional form of  $\chi$  is fundamentally different for dispersive and dissipative coupling (see Supplementary Information). For optical intensity measurement, it is zero when the probe laser is tuned to the cavity resonance, and maximised when it is detuned by  $|\Delta| = \frac{\kappa}{2\sqrt{3}}$ . Conversely, for dissipative coupling,  $|\chi|$  is generally maximised for on-resonance optical driving. This difference is illustrated in Fig. 1b&e.

Fundamentally, photoacoustic sensing is limited by the thermal energy of the gas through which the acoustic wave propagates, which is associated with the first term under the square-root in equation (1). For the characteristic viscous length-scale of our devices ( $l \sim 18$  mm, see Supplementary Information), their area of  $A \sim 0.05$  mm<sup>2</sup>, an ideal pressure participation ratio of  $r = 1$  and a surrounding gas of air at room temperature ( $\mu = 1.8 \times 10^{-5}$  kg/m s) we find this gas-damping thermal limit to be  $P_{\min} \sim 1$   $\mu$ Pa Hz<sup>-1/2</sup>. This predicted fundamental-noise limited sensitivity is many orders of magnitude superior to previously reported ultrasound sensors of comparable size [13]. To reach it, the intrinsic mechanical damping rate ( $\gamma$ ) must be smaller than the gas-damping rate ( $\gamma_{\text{gas}} = \mu l/m$ ), such that a high quality, low mass, mechanical resonator is advantageous. Furthermore, the optical measurement noise must be small enough to allow resolution of the random thermal force from collisions of gas molecules with the resonator. This motivates the use of a small high quality optical cavity, which maximises both the optomechanical susceptibility  $\chi$ , and the intracavity photon number  $N$  for a given incident optical power.

### Sensor design and characterisation

The requirement of high quality optical and mechanical modes in a small-scale sensor aligns closely with microcavity optomechanical devices developed over the past decade to study the quantum physics of nanoscale motion [37, 43]. To this end, here we employ a suspended spoked silica microdisk optomechanical system similar to those reported in

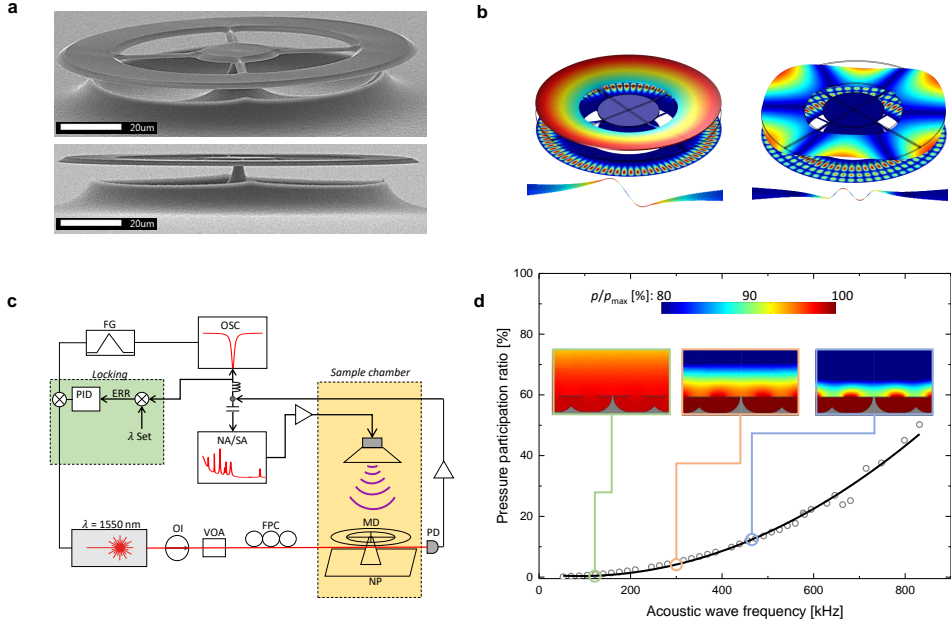


**FIG. 2. Device architecture and experimental schematic.** (a) Scanning electron microgram of the microdisk used in this study. The microdisk is an optical cavity which is evanescently coupled to a tapered optical fibre. Examples of numerically simulated mechanical modes of the tapered fibre as well optical and mechanical modes of the microdisk are shown in (b). (c) Shows the phase sensitive and thermally stabilised experimental setup used to characterise the optomechanical acoustic sensor. NP: nanopositioner; MD: microdisk; PD: photodetector; FPC: fiber polarization controller; VOA: variable optical attenuator; OI: optical isolator; FG: function generator; OSC: digital oscilloscope; NA: network analyser; SA: spectrum analyser. (d) Shows the simulated pressure participation ratio, i.e. the fraction of the total acoustic pressure acting on the mechanical structure, for a number of frequencies. The insets display the pressure distribution at 105, 281 and 421 kHz, respectively; while  $p/p_{\max}$  is the ratio of the pressure to the pressure at the antinodes of the acoustic wave.

Ref. [37], as shown in Fig. 2a. In these structures, the optical field is confined in a high quality whispering-gallery mode around the periphery of the disk; while the use of thin spokes to tether the disk to a silicon substrate isolates the mechanical resonances, resulting in high intrinsic mechanical quality factor without significant sacrifice of sensing area. Moreover, the  $\sim 2 \mu\text{m}$  device thickness ensures a small mass of approximately 220 ng, amplifying the

response to incident ultrasound.

While suspension of the mechanical element offers significant advantages in terms of mechanical quality and compliance, a potential disadvantage is that the underside of the mechanical element is not isolated from the acoustic pressure wave. One might expect this to reduce the pressure difference across the resonator, decreasing the pressure participation ratio and degrading the acoustic sensitivity. To explore this behaviour, we perform finite-element simulations of an acoustic plane wave incident on a spoked silica microdisk, with results shown in Fig. 2d. The participation ratio is found to increase roughly quadratically with acoustic wave frequency, exceeding 50% at frequencies above 800 kHz. We attribute the quadratic dependence firstly to the increasing spatial gradient of the pressure wave with increasing frequency and, secondly, to an increasing resonant confinement of sound between the sensor and the substrate, as the acoustic wavelength becomes comparable to the height of the airgap beneath the sensor.

The spoked microdisk is photolithographically fabricated with outer and inner radii of 150  $\mu\text{m}$  and 80  $\mu\text{m}$ , respectively (see Methods and SEM image in Fig. 2a). The probe laser is evanescently coupled into, and out of, the microdisk via an optical nanofibre, facilitating direct coupling into fibre-optic systems. Both microdisk and tapered fibre support families of mechanical eigenmodes, that can be resonantly driven via an acoustic field (see Fig. 2b for finite element simulations of some typical eigenmodes). The dominant effect of microdisk mode vibration is generally to modify the cavity resonance frequency, providing a mechanism for dispersive optomechanical sensing. On the other hand, vibration of the nanofibre enables dissipative sensing, modifying the distance between fibre and microdisk and therefore the cavity input coupling.

Using the experimental setup shown in Fig. 2c, the mechanical and optical modes of the sensor, as well as its acoustic response, were investigated via their effect on the transmission of the probe laser through the nanofibre. An optical cavity mode with wavelength of around  $\lambda = 1555.7$  nm, in the telecommunications band C-band, and with intrinsic quality factor of  $3.6 \times 10^6$  was selected for the experiments (see Supplementary Fig. 1 and Methods). A feedback loop was used to lock the laser wavelength at a fixed detuning with respect to this mode, such that the experiment was insensitive to low-frequency thermal fluctuations in the cavity and optical fibre circuit and drift of the probe laser wavelength.

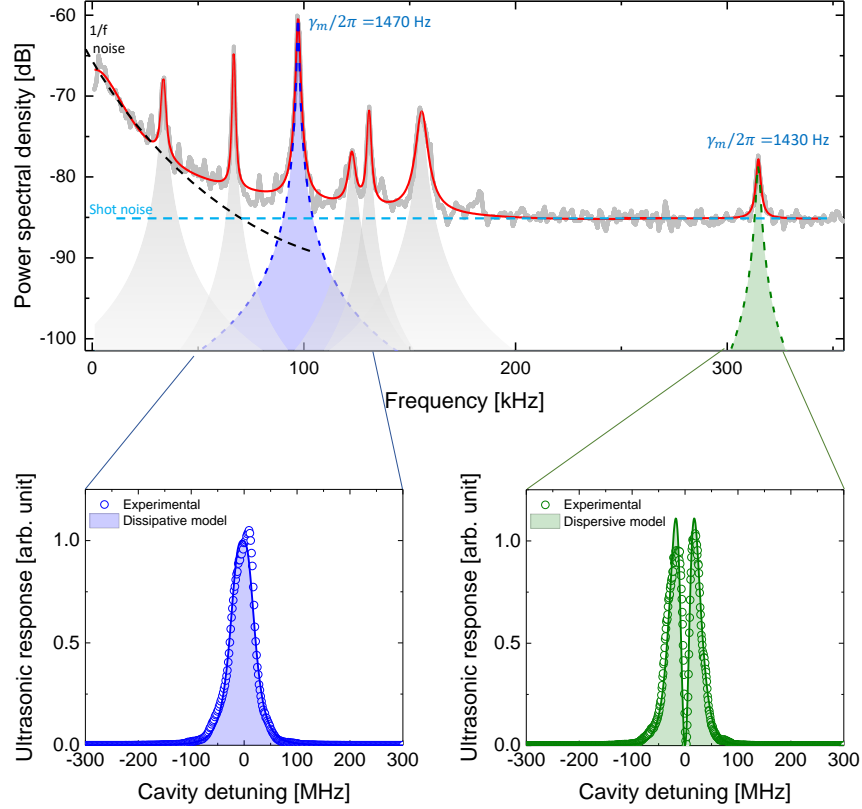


FIG. 3. **Noise spectrum, mechanical modes, and dissipative and dispersive coupling.**

Top panel shows the noise spectral density of the microdisk coupled to the tapered fibre in the absence of acoustic signal. The blue dashed line specifies the shot noise level given by the laser intensity, and the black dashed line corresponds to the  $1/f$  noise. The blue and green shaded areas indicate dispersive and dissipative coupled mechanical modes, respectively, each fitted with a Lorentzian.  $\gamma_m$  quantifies the total mechanical dissipation rate of each of these modes, including both gas damping and intrinsic damping. The bottom panels show the ultrasonic response as a function of laser-cavity detuning at frequencies of 98 kHz and 315 kHz. The shaded areas are fits based upon the theoretical expectation for system response as function of detuning (see Supplementary Information) corresponding to dissipative (left panel) and dispersive (right panel) coupling, respectively.

To investigate the response, noise performance and sensitivity of the sensor, we detuned the laser away from the optical resonance to the point of maximum slope with respect to the cavity dispersion, optimising the dispersive transduction of acoustic signals. The noise spectral density of the sensor was then measured using a spectrum analyser, as shown in

Fig. 3. At low frequencies ( $\lesssim 50$  kHz), the dominant noise mechanism is  $1/f$  noise. At higher frequencies, the noise floor is dominated either by laser shot noise or, near the resonance frequencies of mechanical eigenmodes, thermal force noise with characteristic sharply peaked Lorentzian frequency response.

In order to quantitatively verify our model for cavity optomechanical acoustic sensing (see equation (1) and Fig. 1c and f), we examined the acoustic response for two mechanical modes with resonance frequencies of 98 kHz and 315 kHz, respectively. A piezo-electric element (PZT) was used as an ultrasonic transmitter, creating an ultrasonic wave at each frequency, and the response of the sensor was analysed using a vector network analyser. Specifically, the off-diagonal scattering parameter (i.e., the coherent power transmission from the PZT to the photodetector through the sensor) was recorded as a function of laser-cavity detuning. The results are shown in the bottom panels of Fig. 3. The response of the 98 kHz mechanical mode features a maximum at zero detuning, characteristic of dissipative coupling due to oscillation of the nanofibre (c.f. Fig. 1c); while the response at 315 kHz is zero on cavity resonance, with maxima on either side, characteristic of dispersive coupling due to microdisk vibrations (c.f. Fig. 1f). The results show very good agreement to respective fits to dissipative and dispersive coupling, as shown in Fig. 3, validating the theoretical models for both dissipative and dispersive sensing mechanisms.

### **Characterising the sensor: Dynamic range and sensitivity**

To experimentally quantify the noise equivalent pressure of the sensor, we interferometrically calibrated the displacement of the PZT element as function of its drive frequency. The acoustic pressure generated by the PZT was calculated from its displacement, air acoustic impedance and its distance to the sensor (see Supplement for details). The ultrasonic response of the system was then measured at different frequencies for which the applied pressure was known. Fig. 4a shows the response at 318 kHz, as an example, relative to the shot and thermal force noise. In this example measurement, the thermal force noise dominates shot noise. The signal-to-noise ratio is about  $\text{SNR} = 40$  dB at an electrical bandwidth of  $\Delta f = 200$  Hz and with an applied pressure of  $P_{\text{applied}} = 42$  mPa. The noise equivalent

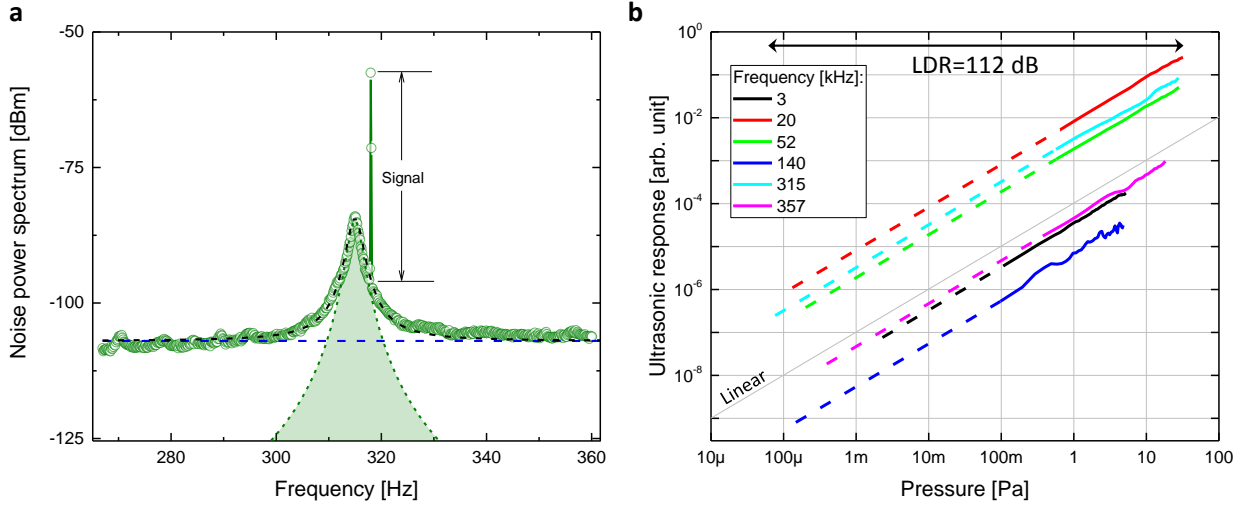


FIG. 4. **Evaluation of the noise equivalent pressure sensitivity and the linear dynamic range (LDR).** (a) Noise spectral density of the sensor near a mechanical mode of the micro-disk measured at an electrical bandwidth of 200 Hz. An ultrasonic pressure of 42 mPa at frequency of 318 kHz is applied to the device resulting in a signal to noise ratio of  $\sim 40$  dB. The shot noise is shown with the dashed blue line. The mechanical motion of the microdisk is fitted with a Lorentzian, introducing the thermal noise shown with the shaded area. The total noise is fitted with the black dash-dot line and is dominated by the thermal noise from 300–330 kHz. (b) Ultrasonic response of the sensor at different frequencies as a function of ultrasonic pressure. The solid grey line is a guide to the eye for a linear response. The LDR is  $>110$  dB at a bandwidth of 1 Hz with its upper limit dictated by the measurement setup rather than the acoustic response. The solid lines correspond to the measured ranges and the dashed lines are extrapolations to the noise equivalent pressure that sets the lower limit of the LDR.

pressure can then be calculated as

$$P_{\min}(\omega) = \frac{P_{\text{applied}}(\omega)}{\sqrt{\Delta f \times \text{SNR}}} \sim 30 \mu\text{Pa}/\sqrt{\text{Hz}}. \quad (2)$$

In comparison, the thermal force noise-dominated noise equivalent pressure predicted from equation (1) is  $20 \mu\text{Pa}/\sqrt{\text{Hz}}$ , given the area and mass of our device, that it operates at room temperature ( $T = 300$  K), our simulated pressure participation ratio at 318 kHz of  $r = 0.055$ , and the measured total mechanical damping rate of  $\gamma_{\text{m}}/2\pi = (\gamma + \gamma_{\text{gas}})/2\pi = 1,430$  Hz. This is in reasonably good agreement, with the discrepancy likely due to the non-ideal overlap of the mechanical modeshape with the profile of the incident pressure wave.

It is informative to examine the contributions to the noise equivalent pressure from intrinsic mechanical dissipation, optical shot noise and fundamental gas damping. As can be seen from Fig. 4, the shot noise power spectrum is 13 dB below the combined thermal force noise from gas and intrinsic damping, contributing 5% in power to the total noise. The fluctuation dissipation theorem dictates that the ratio of noise power introduced by gas damping and intrinsic mechanical damping is equal to the ratio of the damping rates, as may be directly confirmed from equation (1). By measuring the mechanical damping rate as a function of background pressure, we isolated these two components, finding that  $\gamma_{\text{gas}}/2\pi = 1,260$  Hz and  $\gamma/2\pi = 170$  Hz (see Supplementary Information). The gas damping noise power therefore dominates by a factor of  $\gamma_{\text{gas}}/\gamma \sim 7.4$ . All-in-all, these results show that, at this acoustic frequency, the noise equivalent pressure of the sensor is within 9% of the noise floor introduced by thermal collisions of gas molecules with the sensing element. This gas damping noise floor is fundamental, in that it cannot be eliminated without removing the medium through which the acoustic wave itself propagates. To our knowledge, our sensor is the first acoustic sensor which is sufficiently sensitive for it to dominate.

To explore the bandwidth of the sensor, we performed a broadband measurement of the pressure sensitivity from 1 kHz to 1 MHz (see Supplementary Fig. 4), achieving narrowband sensitivities of 10–100  $\mu\text{Pa}/\sqrt{\text{Hz}}$  for many frequencies across this range. The upper limit of 1 MHz is not intrinsic, but rather introduced by the inability to generate acoustic waves at higher frequencies due to the frequency response of our PZT transducer and the high acoustic attenuation of air at high frequencies. While the device was not optimised for audio frequencies, its performance at these frequencies remained sufficient to record the Chris Jones song “Long After You’re Gone” in the lab environment by digitizing the output of the photo-detector with no further processing and filtering (see online Supporting Information, Video 1).

To investigate how the ultrasonic response changes when varying the magnitude of the acoustic pressure, we recorded the system response at various frequencies as a function of the applied pressure up to the maximum of  $\sim 30$  Pa accessible using our experimental setup. Results are shown in Fig. 4b. We found that the ultrasonic response scales linearly with applied pressure throughout the accessible pressure range. A lower bound on the linear dynamic range (LDR) can then be evaluated from the lower limit of the response (given by the noise equivalent pressure sensitivity and electrical bandwidth) and the maximum

applied pressure. As shown in Figure 4b, the sensor had a LDR  $> 112$  dB at a measurement bandwidth of 1 Hz.

## Discussion

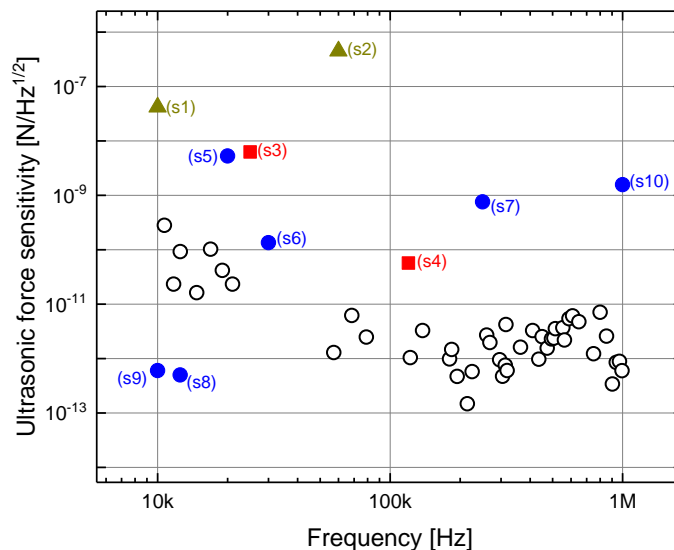


FIG. 5. **Ultrasonic force sensitivity in comparison with other sensors.** Ultrasonic force sensitivity is evaluated from the noise equivalent pressure sensitivity normalized to the sensing area and plotted versus frequency: open circles correspond to this work and other symbols show results of other approaches including optical (solid circles), capacitive (solid rectangles) and piezoelectric (solid triangles). The improvement of the sensitivity in this work is especially notable between 200 kHz to 1 MHz. Citations to previous work are provided in the Supplementary Information.

It is interesting to compare the sensitivity of our sensor with existing ultrasound sensors. The absolute sensitivity represents a five order-of-magnitude advance on previous optical acoustic sensors based on non-suspended microring resonators [38, 39] which sense pressure via a change in optical refractive index, rather than driven mechanical motion. More broadly, as a general rule the sensitivity improves as  $A^{-1}$  (see equation (1)) since increasing the area of the device increases the force exerted on it by a given pressure wave. Therefore a good measure for comparing sensors of different dimensions is the pressure sensitivity normalized to the sensing area, or the *ultrasonic force sensitivity*. Fig. 5 compares the ultrasonic force sensitivity of our sensor to that of other ultrasound sensors over the frequency range from

10 kHz to 1 MHz, showing superior performance. The performance is especially good at frequencies between 200 kHz and 1 MHz, where the noise equivalent pressure represents an advance of more than three orders-of-magnitude. The sensor could be scaled straightforwardly to larger or smaller sizes, for improved absolute pressure sensitivity or improved resolution/high frequency sensitivity, respectively.

The sensitivity could be further improved by engineering the physical structure of the device to both increase the pressure participation ratio, and decrease the noise contribution from collisions with thermal gas molecules. The participation ratio can be optimised, for a given acoustic wave frequency, by controlling the height of the sensor above the silicon substrate. Indeed, our modelling suggests that participation ratios even exceeding  $r = 1$  are achievable due to resonant enhancement of the pressure wave between the substrate and device. This, in effect, would represent a microscale acoustic resonator fabricated on a silicon chip, with significant advantages over the bulk-machined acoustic resonators often used to enhance acoustic pressure waves in other approaches [2]. The noise contribution from thermal gas molecule collisions is determined by the geometry-dependent characteristic length-scale  $l$ , which includes the effects of both squeeze-film molecular damping and air-drag damping. In our case the squeeze film damping dominates by approximately a factor of two (see Supplementary Information). Squeeze-film damping scales with inverse-height cubed and both damping mechanisms scale with the mass of the resonator. By increasing the separation of the device from the substrate, to reach the air-drag damping dominated regime and to enhance the participation ratio, and by thinning the resonator to about 300 nm, the sensitivity could be improved by more than a factor of fifty, reaching the sub-micropascal regime (see Supplementary Information).

The improved ultrasound sensitivity and microscale resolution offered by our new acoustic sensing technique has prospects for a range of applications. For instance, it could allow improved sensitivity and resolution in photoacoustic imaging [9]; improved navigation and spatial imaging in unmanned and autonomous vehicles [44]; and higher sensitivity high resolution photoacoustic trace gas sensing [2]. In trace gas sensing, the sensitivity reported here could allow detection of carbon dioxide at part-per-billion concentrations with unprecedented spatial resolution (See Supplementary Information). This could, for example, enable measurements of the respiration of individual cells and bacteria, such as photosynthesis and gas exchange through the cell membrane [45, 46]. Our sensor could also be applied

to observe acoustic waves generated by the nanoscale vibrations associated with cellular metabolism [18]. Measurements of these vibrations have been shown to allow diagnostic assays of cellular toxicity and antibiotic resistance [18], and provide insight into molecular processes such as conformational changes [48]. Unlike current atomic force microscope-based approaches [18], our sensor could allow these measurements to be performed without physical contact, and therefore without disrupting the observed processes or contaminating the sensor. Moreover, the measurements could be performed with higher bandwidth, and resolve nanometer-level cellular vibration amplitudes at low kilohertz frequencies and sub-picometer vibrations at above 100 kHz (see Supplementary Information).

One potential drawback of our technique is that it relies on mechanical resonances. While able to operate simultaneously on multiple mechanical resonances over the full 10 kHz to 1 MHz frequency band, it is inherently narrowband around each of these resonances. We observe that many – perhaps indeed most – applications function by generating and then measuring monochromatic acoustic waves, and can therefore be tuned to the known mechanical resonances of the sensor. Never-the-less, broadband sensitivity may be possible in future devices by using increased optical power or stronger optomechanical coupling to suppress the optical shot noise (see equation (1)), together with laser or feedback cooling to broaden the mechanical resonances without introducing additional thermal noise [26–29]. A second challenge for applications such as photoacoustic imaging and underwater sonar will be to extend the technique to liquid environments. To this end, we observe that high quality mechanical resonances have recently been observed in similar device structures within a liquid [49]. This suggests that operation in liquid is feasible.

## Methods

**Device fabrication:** The spoked microdisks were fabricated on silicon wafers, covered with a 2  $\mu\text{m}$  layer of thermally grown silicon dioxide. The wafer was first coated with photoresist and spoked circular pads were defined using UV-photolithography (see Supplementary Fig. 5a). After developing the photoresist, the wafer was exposed to buffered Hydrofluoric acid, removing all the uncovered silicon dioxide (see Supplementary Fig. 5b)). The remaining photoresist was consecutively cleaned off with acetone (see Supplementary Fig. 5c). In the subsequent step, the wafer was coated again with photoresist for protection

and mechanically separated into about 30 chips containing 10 circular silicon dioxide structures each. After separation, the photoresist was removed and the chips were individually exposed to XeF<sub>2</sub> gas, selectively removing the silicon and releasing the silica structures (see Supplementary Fig. 5d and e).

**Characterisation setup:** Light from a 1555 nm tunable Erbium-doped fiber laser [NKT Photonics, Koheras Adjustik] was guided to the experiment through an optical isolator to avoid reflection back into the laser. The intensity of the laser was adjusted using a variable fiber attenuator. The frequency of the laser could be thermally tuned over a range of about one nm or electronically swept over tens of picometers using a built-in piezo element of the laser cavity. The polarization of the light was adjusted using a fiber polarization controller (FPC). A tapered nanofibre was used to evanescently couple the laser to a whispering-gallery-mode of the disk. The crucial coupling distance between the taper and the disk was coarsely adjusted using manual micrometer stages and optical microscopes. Fine-tuning was implemented using a nanopositioning stage [Thorlabs MDT693A]. The transmitted light was detected with an InGaAs-photodetector [New Focus 1811 DC-125MHz].

**Optical mode characterisation:** The optical mode of the microdisk was investigated by measuring the transmission of the probe laser as a function of the laser frequency. The frequency of the laser ( $\lambda = 1555.716$  nm) was swept over the cavity optical mode using a function generator (FG) and the probed laser transmission was recorded with an oscilloscope (OSC) (see Fig. 2c). The optical mode was found to have a quality factor  $Q = 1.8 \times 10^6$  when the tapered fibre was positioned so that the input optical coupling rate matched the intracavity loss rate, i.e. critical coupling (see Supplementary Fig. 1). This implies an intrinsic quality factor of  $3.6 \times 10^6$ .

**Noise floor and signal response:** The high-frequency part of the signal was Fourier transformed in a spectrum analyser [Agilent N9010A] to analyse the sensor noise spectrum, and to calibrate the sensor signal to noise ratio (SNR). The system network response was measured using a vector network analyser [Agilent E5061B] to determine the dependence of the SNR on applied acoustic pressure and to determine sensitivity as a function of frequency. The Network analyser was also used to calibrate a piezo element (Thorlabs AE0505D08F) as a function of frequency and voltage to operate as the acoustic source (see Supplementary Information for detail).

### **Author contributions**

WPB provided overall leadership for the project. SB, AA and WPB conceptualized the idea and designed the experiments. SB and AA set up the experiments, performed the measurements and analyzed the data. All co-authors interpreted the data. SF and SB fabricated the devices. SB and WPB developed the theoretical model. SB and SF performed the finite element simulations. All co-authors contributed in the development of the manuscript which was initially drafted by SB and AA.

### **Acknowledgments**

Authors would like to thank Glen Harris and Xin He for their help with experiments and Chris Baker for his help with finite element simulations. The project was funded primarily by the Australian Research Council through the Discovery Project DP140100734. WPB acknowledges an Australian Research Council Future Fellowship (FT140100650). SB acknowledges funding from the European Unions Horizon 2020 research and innovation programme under the Marie Skłodowska-Curie grant agreement No 663830. AA is a Sêr Cymru II Rising Star Fellow.

### **Additional information**

- 
- [1] Wang, L. V. & Hu, S. Photoacoustic tomography: in vivo imaging from organelles to organs. *Science*, **335**, 1458-1462 (2012).
- [2] Wu, H. et al. Beat frequency quartz-enhanced photoacoustic spectroscopy for fast and calibration-free continuous trace-gas monitoring, *Nat. Commun.* **8**, 15331 (2017).
- [3] Fischer, B. *Nat. Photon.*, **10**, 356-358 (2016).
- [4] Lang, C., Fang, J., Shao, H., Ding, X. & Lin, T. High-sensitivity acoustic sensors from nanofibre webs. *Nat. Commun.*, **7**, (2016).
- [5] Scheeper, P. R., van der Donk, A. G. H., Olthuis, W. & Bergveld, P. A review of silicon microphones. *Sensor. Actuat. A-Phys.* **44**, 111 (1994).
- [6] Chan, C. K., Lai, W.C., Wu, M., Wang, M.Y. & Fang, W. Design and implementation of a capacitive-type microphone with rigid diaphragm and flexible spring using the two poly silicon micromachining processes. *IEEE Sens. J.*, **11**, 2365-2371 (2011).
- [7] Wolfbeis, O. S. Fiber-optic chemical sensors and biosensors. *Anal. chem.* **80**, 4269-4283 (2008).
- [8] Razansky, D. et al. Multispectral opto-acoustic tomography of deep-seated fluorescent proteins in vivo. *Nat. Photon.* **3**, 412 (2009).
- [9] Wang, L. V. Multiscale photoacoustic microscopy and computed tomography. *Nat. Photon.*, **3**, 503 (2009).
- [10] Consales, M. et al. Lab-on-fiber technology, toward multifunctional optical nanoprobe. *ACS Nano*, **6**, 31633170 (2012).
- [11] Ballantine Jr, D. S. et al. *Acoustic Wave Sensors: Theory, Design and Physico-Chemical Applications* (Elsevier, 1996).
- [12] Preisser, S. All-optical highly sensitive akinetic sensor for ultrasound detection and photoacoustic imaging. *Biomed. Opt. Express*, **7**, 4171-4186 (2016).
- [13] Guggenheim, J. A. et al. Ultrasensitive plano-concave optical microresonators for ultrasound sensing. *Nat. Photon.* **11**, 714 (2017).
- [14] Anetsberger, G. et al. Near-field cavity optomechanics with nanomechanical oscillators. *Nat. Phys.* **5**, 909 (2009).
- [15] Wu, M. et al. Dissipative and dispersive optomechanics in a nanocavity torque sensor. *Phys. Rev. X*, **4**, 021052 (2014).

- [16] Arcizet, O. et al. High-sensitivity optical monitoring of a micromechanical resonator with a quantum-limited optomechanical sensor. *Phys. Rev. Lett.* **97**, 133601 (2006).
- [17] Carmon, T., Rokhsari, H., Yang, L., Kippenberg, T.J. & Vahala, K.J. Temporal behavior of radiation-pressure-induced vibrations of an optical microcavity phonon mode. *Phys. Rev. Lett.* **94**, 223902 (2005).
- [18] Eichenfield, M., Chan, J., Camacho, R. M., Vahala, K. J. & Painter, O. Optomechanical crystals. *Nature* **462**, 78 (2009).
- [19] Bowen, W.P. & Milburn, G.J. *Quantum Optomechanics* (CRC Press, 2015).
- [20] Abbott, B. P. et al. LIGO: the laser interferometer gravitational wave observatory. *Rep. Prog. Phys.*, **72**, 076901 (2009).
- [21] Abbott, B. P. et al. GW151226: Observation of gravitational waves from a 22-solar-mass binary black hole coalescence. *Phys. Rev. Lett.* **116**, 241103 (2016).
- [22] Krause, A. G., Winger, M., Blasius, T. D., Lin, Q. & Painter, O. A high-resolution microchip optomechanical accelerometer. *Nat. Photon.* **6**, 768-772, (2012).
- [23] Forstner, S. et al. Cavity optomechanical magnetometer. *Phys. Rev. Lett.*, **108**, 120801 (2012).
- [24] Gavartin, E., Verlot, P. & Kippenberg, T. J. A hybrid on-chip optomechanical transducer for ultrasensitive force measurements. *Nat. Nanotechnol.* **7**, 509-514 (2012).
- [25] Basiri-Esfahani, S., Myers, C. R., Armin, A., Combes, J., & Milburn, G. J. Integrated quantum photonic sensor based on Hong-Ou-Mandel interference. *Opt. Express*, **23**, 16008-16023 (2015).
- [26] Teufel, J. D. et al. Sideband cooling of micromechanical motion to the quantum ground state. *Nature*, **475**, 359 (2011).
- [27] Chan, J. et al. Laser cooling of a nanomechanical oscillator into its quantum ground state. *Nature*, **478**, 89 (2011).
- [28] Schliesser, A. et al. Resolved-sideband cooling of a micromechanical oscillator. *Nat. Phys.*, **4**, 415 (2008).
- [29] Lee, K. H., McRae, T. G., Harris, G. I., Knittel, J., & Bowen, W. P. Cooling and control of a cavity optoelectromechanical system. *Phys. Rev. Lett.* **104**, 123604 (2010).
- [30] Riedinger, R. et al. Non-classical correlations between single photons and phonons from a mechanical oscillator. *Nature*, **530**, 313 (2016).
- [31] Wollman, E. E. et al. Quantum squeezing of motion in a mechanical resonator. *Science*, **349**, 952-955 (2015).

- [32] Basiri-Esfahani, S., Akram, U. & Milburn, G. J. Phonon number measurements using single photon opto-mechanics. *New J. Phys.*, **14**, 085017 (2012).
- [33] Bennett, C. H. & DiVincenzo, D. P. Quantum information and computation. *Nature* **404**, 247 (2000).
- [34] Nielsen, M. A. & Chuang, I. L. *Quantum Computation and Quantum Information* (Cambridge university press, 2010).
- [35] Basiri-Esfahani, S., Myers, C. R., Combes, J. & Milburn, G. J. Quantum and classical control of single photon states via a mechanical resonator. *New J. Phys.*, **18**, 063023 (2016).
- [36] Milburn, G. J. & Basiri-Esfahani, S. Quantum optics with one or two photons. *Proc. R. Soc. A* **471**, 20150208 (2015).
- [37] Anetsberger, G., Rivière, R., Schliesser, A., Arcizet, O., & Kippenberg, T. J. Ultralow-dissipation optomechanical resonators on a chip. *Nat. Photon.*, **2**, 627 (2008).
- [38] Li, H., Dong, B., Zhang, H.F. & Sun, C. A transparent broadband ultrasonic detector based on an optical micro-ring resonator for photoacoustic microscopy, *Sci. Rep.* **4**, 4496 (2014).
- [39] Ling, T., Chen, S.-L. & Guo, L.J. High-sensitivity and wide-directivity ultrasound detection using high Q polymer microring resonators, *Appl. Phys. Lett.* **98**, 204103 (2011).
- [40] Thompson, J.D. et al. Strong dispersive coupling of a high-finesse cavity to a micromechanical membrane. *Nature*, **452**, 72-75 (2008).
- [41] Xuereb, A., Schnabel, R. & Hammerer, K. Dissipative optomechanics in a Michelson-Sagnac interferometer. *Phys. Rev. Lett.*, **107**, 213604 (2011).
- [42] Knittel, J., Jong, J.H., Gray, M.B., Taylor, M.A. & Bowen W.P., Ultrasensitive real-time measurement of dissipation and dispersion in a whispering-gallery mode microresonator. *Opt. Lett.* **38**, 1915-1917 (2013).
- [43] Jiang, X., Lin, Q., Rosenberg, J., Vahala, K., & Painter, O. High-Q double-disk microcavities for cavity optomechanics. *Opt. Express*, **17**, 20911-20919 (2009).
- [44] Schmid, K., Lutz, P., Tomić, T., Mair, E., & Hirschmüller, H. Autonomous Visionbased Micro Air Vehicle for Indoor and Outdoor Navigation. *J. F. Robot.*, **31**, 537-570 (2014).
- [45] Ho, Q. T., Verboven, P., Yin, X., Struik, P. C., & Nicolai, B. M. A microscale model for combined CO<sub>2</sub> diffusion and photosynthesis in leaves. *PloS One*, **7**, e48376 (2012).
- [46] Oswald, R. et al. HONO emissions from soil bacteria as a major source of atmospheric reactive nitrogen. *Science*, **341**, 1233-1235 (2013).

- [47] Longo, G. et al. Rapid detection of bacterial resistance to antibiotics using AFM cantilevers as nanomechanical sensors. *Nat. Nanotechnol.* **8**, 522 (2013).
- [48] Alonso-Sarduy, L. et al. Real-time monitoring of protein conformational changes using a nanomechanical sensor. *PloS One*, **9**, e103674 (2014).
- [49] Gil-Santos, E. et. al. High-frequency nano-optomechanical disk resonators in liquids. *Nat. Nanotechnol.* **10**, 810-816 (2015).

# SUPPLEMENTARY INFORMATION

## I. CHARACTERISING THE OPTICAL RESONANCE

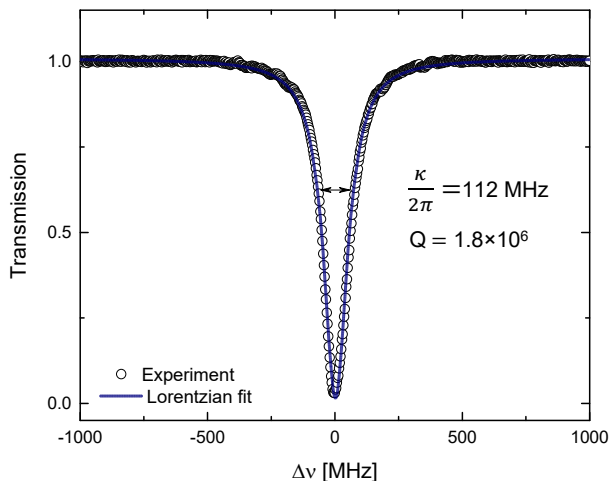


FIG. 1. **Optical resonance.** One of the optical modes of the micro-disk ( $\lambda = 1555.716$  nm) is shown with optical quality factor and cavity damping indicated on the figure.

The optical resonance used in the experiments was characterised by scanning the frequency of the laser across the mode and fitting the observed transmission through the tapered fibre to an inverted Lorentzian (see Fig. 1). This allowed the coupled cavity decay rate  $\kappa$  and quality factor  $Q$  to be determined. These were found to be  $\kappa = 112$  MHz and  $Q = 1.8 \times 10^6$ .

## II. REFERENCES TO PREVIOUS ULTRASOUND SENSORS

Fig. 5 in the main text compares the ultrasonic force sensitivity of our sensor to prior results. The prior results are labelled “sx” where the “s” is used to refer to the Supplement, and the numbers  $x$  refer to Supplementary Information references [1]–[10].

### III. DERIVATION OF THE NOISE EQUIVALENT PRESSURE SENSITIVITY

We start by modelling the motion of a single mode mechanical oscillator at room temperature in response to an external acoustic drive, and probed by a coherent field. In regime where the mechanical thermal noise dominates on resonance, and the quantum back-action noise on the sensor is negligible, we can take the high temperature limit where  $\bar{n}(\omega) = k_{\text{B}}T/\hbar\omega$ . In this regime, we obtain an optical shot-noise limited noise force floor. The Langevin equations of motion for the mechanical displacement and the optical cavity mode respectively are written as

$$m \frac{d^2 x_{\text{m}}(t)}{dt^2} + m\gamma \frac{dx_{\text{m}}(t)}{dt} + kx_{\text{m}}(t) = F_{\text{T}} + F_{\text{D}}(t), \quad (3)$$

$$\frac{da(t)}{dt} = -\frac{i}{\hbar}[a, H_{\text{sys}}] - \frac{\kappa}{2}a(t) + \sqrt{\kappa_{\text{in}}}a_{\text{in}} + \sqrt{\kappa_{\text{l}}}a_{\text{l}}, \quad (4)$$

in which  $k$  is the spring constant,  $F_{\text{T}} = \sqrt{2m\gamma k_{\text{B}}T}$  is the thermal force,  $\gamma$  is the mechanical damping rate,  $F_{\text{D}}(t) = rP_{\text{D}}(t)A$  is the acoustic drive force in which  $r$  is the pressure participation ratio defined in the main text,  $P_{\text{D}}$  is the acoustic pressure and  $A$  is the sensing area;  $\kappa_{\text{in}}$  is the input coupling of the cavity to the input optical field,  $\kappa_{\text{l}}$  is the intrinsic cavity loss and  $\kappa = \kappa_{\text{in}} + \kappa_{\text{l}}$ . Moreover,  $H_{\text{sys}} = \hbar\Delta_{\text{c}}a^{\dagger}a + \hbar g_0 a^{\dagger}a x_{\text{m}}$  is the Hamiltonian of the system in the interaction picture rotating with the frequency of the laser in which the optical detuning  $\Delta_{\text{c}} = \Delta + g_{\text{disp}}x_{\text{m}} + O^2 + \dots$ , includes the dispersive coupling due to the presence of the mechanical oscillation.  $\kappa_{\text{in}} = \kappa_{\text{in},0}(1 - g_{\text{diss}}x_{\text{m}})$  includes the dissipative coupling of the input field to the cavity in response to the acoustic field up to the first order in  $x_{\text{m}}$ .  $a_{\text{in}}$  and  $a_{\text{l}}$ , respectively, show the input optical field into the cavity and the vacuum input noise. In case where the input optical field is a semi-classical coherent laser field, we can displace the amplitude of the optical field such that  $a \rightarrow \bar{a} + \alpha_{\text{in}}$  where  $|\alpha_{\text{in}}|^2 = N$  is the input photon intensity.

The solution to equation (3) in Fourier transformed frequency domain is

$$x_{\text{m}}(\omega) = \chi_{\text{m}}(\omega)[F_{\text{T}} + F_{\text{D}}(\omega)], \quad (5)$$

in which the mechanical susceptibility  $\chi_{\text{m}}$  is calculated as  $\chi_{\text{m}}^{-1} = m(\omega_{\text{m}}^2 - \omega^2 - i\gamma_{\text{m}}\omega)$ , where  $m$  and  $\omega_{\text{m}}$  are respectively the mass and the resonance frequency of the mechanical object. The output cavity mode,  $a_{\text{out}}$  is related to the cavity mode,  $a$ , and the input mode into the cavity,  $a_{\text{in}}$ , through the input-output relation [11, 12],  $a_{\text{out}} = \sqrt{\kappa_{\text{in}}}a - a_{\text{in}}$ . By solving equation

(3), the motional displacement of the mechanical resonator or the fiber can be calculated. Moreover, equation (4) can be solved in the frequency domain in linearised displacement regime to get the cavity mode  $a$ . Using the solutions to equations (3,4) together with the input-output relation, the output field of the cavity is calculated as

$$a_{\text{out}}(\omega) = (B(\omega) - C(\omega))x_m(\omega) + D(\omega)a_{\text{in}} + E(\omega)a_l, \quad (6)$$

in which

$$\begin{aligned} B(\omega) &= \frac{-2i\alpha_{\text{in}}g_{\text{disp}}\kappa_{\text{in},0}}{(\kappa_0 + 2i\Delta)(\kappa_0 + 2i(\Delta - \omega))}, \\ C(\omega) &= \frac{2\alpha_{\text{in}}g_{\text{diss}}\kappa_{\text{in},0}}{\kappa_0 + 2i(\Delta - \omega)} \left(1 - \frac{2\kappa_{\text{in},0}}{\kappa_0 + 2i\Delta}\right), \\ D(\omega) &= \frac{\kappa_{\text{in},0} - \kappa_l - 2i(\Delta - \omega)}{\kappa_0 + 2i(\Delta - \omega)}, \\ E(\omega) &= \frac{\sqrt{\kappa_{\text{in},0}\kappa_l}}{\kappa_0 + 2i(\Delta - \omega)}, \end{aligned} \quad (7)$$

in which  $\kappa_{\text{in},0}$  is the original value of the input coupling in absence of the acoustic pressure,  $\kappa_0 = \kappa_{\text{in},0} + \kappa_l$ ,  $g_{\text{disp}} = \frac{d\Delta}{dx}$  is the dispersive coupling rate and  $g_{\text{diss}} = \frac{1}{\kappa_{\text{in},0}} \frac{d\kappa_{\text{in}}}{dx}$  is the dissipative coupling rate. Hence, in the regime where  $|\alpha_{\text{out}}| \gg |\bar{a}|$ , the output intensity of the cavity can be calculated as  $I_{\text{out}}(\omega) \sim \alpha_{\text{out}}^* a_{\text{out}}(\omega) + \alpha_{\text{out}} a_{\text{out}}^\dagger(-\omega)$  where  $\alpha_{\text{out}} = |\alpha_{\text{out}}| e^{i\varphi}$  is the average amplitude of the output field. The intensity can be rewritten as  $I_{\text{out}}(\omega) \sim |\alpha_{\text{out}}| X_{\text{out}}^\varphi(\omega)$ , in which  $X_{\text{out}}^\varphi(\omega)$  is defined as the amplitude quadrature of the output field fluctuations as  $X_{\text{out}}^\varphi(\omega) = a_{\text{out}}(\omega) e^{-i\varphi} + a_{\text{out}}^\dagger(-\omega) e^{i\varphi}$ . As for the rest of the calculations we require the output fluctuations, we normalize the output intensity as  $I_{\text{out}}(\omega) \rightarrow \frac{I_{\text{out}}(\omega)}{|\alpha_{\text{out}}|} \sim X_{\text{out}}^\varphi(\omega)$ . For the case of having only dispersive coupling where we assume  $g_{\text{diss}} = 0$  we get

$$\begin{aligned} X_{\text{out}}^\varphi(\omega)|_{\text{disp}} &= \chi_m(\omega)(e^{-i\varphi}B(\omega) + e^{i\varphi}B^*(\omega))F_T + \chi_m(\omega)A(e^{-i\varphi}B(\omega) + e^{i\varphi}B^*(\omega))rP_D(\omega) \\ &\quad + |D(\omega)|X_{\text{in}}^\theta + |E(\omega)|X_l^\phi, \end{aligned} \quad (8)$$

where we have used this convention in the Fourier frequency domain that  $[a(\omega)]^\dagger = a^\dagger(-\omega)$ .

For the case of having only dissipative coupling where we assume  $g_{\text{disp}} = 0$  we have

$$\begin{aligned} X_{\text{out}}^\varphi(\omega)|_{\text{diss}} &= \chi_m(\omega)(e^{-i\varphi}C(\omega) + e^{i\varphi}C^*(\omega))F_T + \chi_m(\omega)A(e^{-i\varphi}C(\omega) + e^{i\varphi}C^*(\omega))rP_D(\omega) \\ &\quad + |D(\omega)|X_{\text{in}}^\theta + |E(\omega)|X_l^\phi. \end{aligned} \quad (9)$$

The area of the sensor,  $A$ , is respectively the area of the disk in equation (8),  $A = A_m$ , and the area of the fiber in equation (9),  $A = A_f$ .

Based on the above mentioned convention,  $[a(\omega)]^\dagger = a^\dagger(-\omega)$ , the power spectrum of the observable,  $X_{\text{out}}$ , is defined as [13]

$$\begin{aligned} S_{X_{\text{out}}X_{\text{out}}}(\omega) &= \int_{-\infty}^{\infty} d\omega' \langle X_{\text{out}}^\dagger(-\omega) X_{\text{out}}(\omega') \rangle \\ &= \int_{-\infty}^{\infty} d\omega' \langle (a(\omega)a^\dagger(-\omega))(a^\dagger(-\omega')a(\omega')) \rangle. \end{aligned} \quad (10)$$

The power spectrum,  $S_{X_{\text{out}}X_{\text{out}}}$ , can be used to calculate the noise equivalent pressure sensitivity. Considering a signal to noise ratio (SNR) equal to unity, the noise power spectrum becomes

$$S_{\text{PP}} \left[ \frac{\text{Pa}^2}{\text{Hz}} \right] = \frac{1}{r^2 A^2} \left( 2m\gamma k_{\text{B}}T + \frac{1}{N|\chi(\omega)|^2} \right), \quad (11)$$

where we define  $\chi(\omega)$  as the *optomechanical susceptibility*, which depends on the particulars of the coupling regime. For dispersive coupling it is

$$\chi(\omega) = \frac{32g_{\text{disp}}\Delta\kappa_{\text{in},0}\chi_{\text{m}}(\omega)(\kappa_0 - i\omega)}{(4\Delta^2 + \kappa_0^2)(4\Delta^2 + (\kappa_0 - 2i\omega)^2)}. \quad (12)$$

For dissipative regime it is

$$\chi(\omega) = \frac{[2g_{\text{diss}}\kappa_{\text{in},0}(-\kappa_0(\kappa_{\text{in},0} - \kappa_1)(\kappa_0 - 2i\omega) + 4\Delta^2(\kappa_0 + 2\kappa_{\text{in},0} - 2i\omega)] \chi_{\text{m}}(\omega)}{(4\Delta^2 + \kappa_0^2)(4\Delta^2 + (\kappa_0 - 2i\omega)^2)}, \quad (13)$$

is the optical susceptibility.

For the valid regime in this work,  $\omega \ll \kappa$ , the optomechanical susceptibility reduces to a simpler form of

$$\chi(\omega) = \frac{2g_i\kappa_{\text{in},0}\chi_{\text{m}}(\omega)}{(4\Delta^2 + \kappa_0^2)^2} \times C^i, \quad (14)$$

where  $i \in \{\text{disp}, \text{diss}\}$ ,  $C^{\text{disp}} = 16\kappa_0\Delta$  and  $C^{\text{diss}} = -\kappa_0^2(\kappa_{\text{in},0} - \kappa_1) + 4\Delta^2(\kappa_0 + 2\kappa_{\text{in},0})$ .

#### IV. SENSOR RESPONSE

In equations (8) and (9), the coefficient in front of the external drive force by the applied pressure,  $P_d(\omega)$ , is the response of the system. In Fig. 2, we have plotted the system response versus detuning for both dispersive and dissipative regimes.

#### V. UTILISING A MICHELSON INTERFEROMETER TO CALIBRATE THE PIEZOELECTRIC SOUND SOURCE

To calibrate the piezo element (PZT1), we attached to it a light weight silver mirror ( $M_1$ ) which is utilized as a mirror to be displaced in one of the arms of a Michelson interferometer

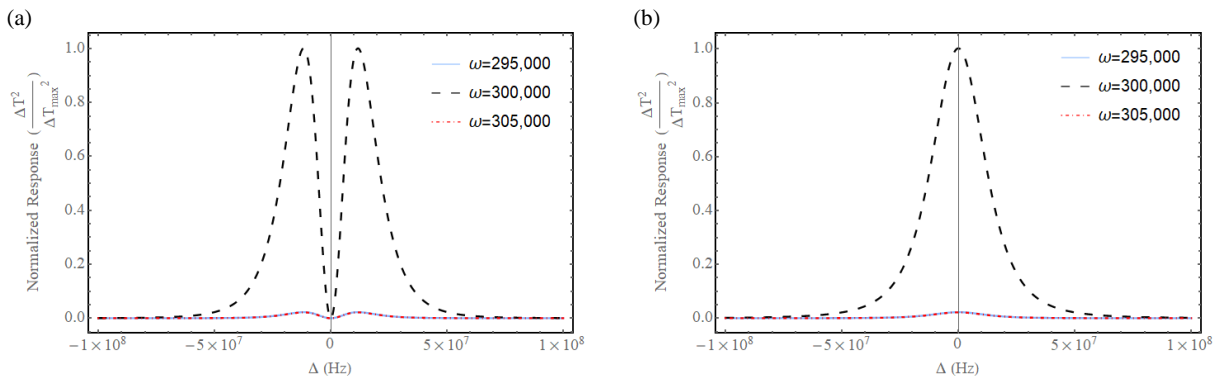


FIG. 2. **Sensor response versus detuning of the laser from cavity resonance frequency.**

Plots are done for  $\kappa_1 = 4 \times 10^7$ ,  $\kappa_{in} = 0.5 \times 10^6$ ,  $T = 293^\circ\text{K}$  and  $N = 25 \times 10^{14}$ , (a) For the case where we assume that  $\delta x_f = 0$  and the sensor operates in pure dispersive opto-mechanical regime. The plot is done for the real size of the disk resonator used in the experiment for which thickness of the disk= $2\mu\text{m}$ , external radius= $150\mu\text{m}$ , internal radius= $80\mu\text{m}$ . which results in a mass of  $m=3.1 \times 10^{-10}$  kg and area of  $A_m = 5 \times 10^{-8}\text{m}^2$  for the silica disk resonator with  $\omega_m = 300$  kHz,  $\gamma_m = 1500$  Hz and  $g_{disp} = 10^{14}$ . (b) for sensor operating in pure dissipative coupling where the length of the tapered fiber is 0.5 mm with a radius of 500 nm which results in  $A_f = 7.85 \times 10^{-10}\text{m}^2$  and a mass of  $m=10^{-12}$  kg. We assume the same resonance frequency and mechanical damping rate of  $\omega_m = 300$  kHz and  $\gamma_m = 1500$  Hz respectively as for the dispersive case, and  $g_{diss} = 5 \times 10^8$ .

as shown in Fig. 3a. The interferometer is fed by a laser at  $\lambda \simeq 1555$  nm and the output interference signal is detected on a low noise photodetector as shown in the experiment scheme. We used a secondary PZT element (shown as Phase control PZT in Fig. 3a) with a mirror attached to it in the other interferometer arm to thermally lock its phase using a PID (proportional integral derivative) controller.

To perform the measurement, we used a network analyser with its port 1 driving the PZT1 (DUT) and port 2 receives the signal from the PD. The PI-controller output is connected to PZT2 (phase control) through a voltage amplifier (Falco Sytems WMA-300). The displacement spectrum of PZT1 can be calculated as

$$d(\omega) = \frac{\lambda V(\omega_{ref})}{4 V_{max}} \sqrt{\frac{S_{21}(\omega)}{S_{21}(\omega_{ref})}}, \quad (15)$$

where  $S_{21}(\omega)$  is the off-diagonal network scattering parameter corresponding to the coherent power transfer from port 1 to port 2 at a frequency  $\omega$ .  $\omega_{ref}$  is a calibration reference frequency

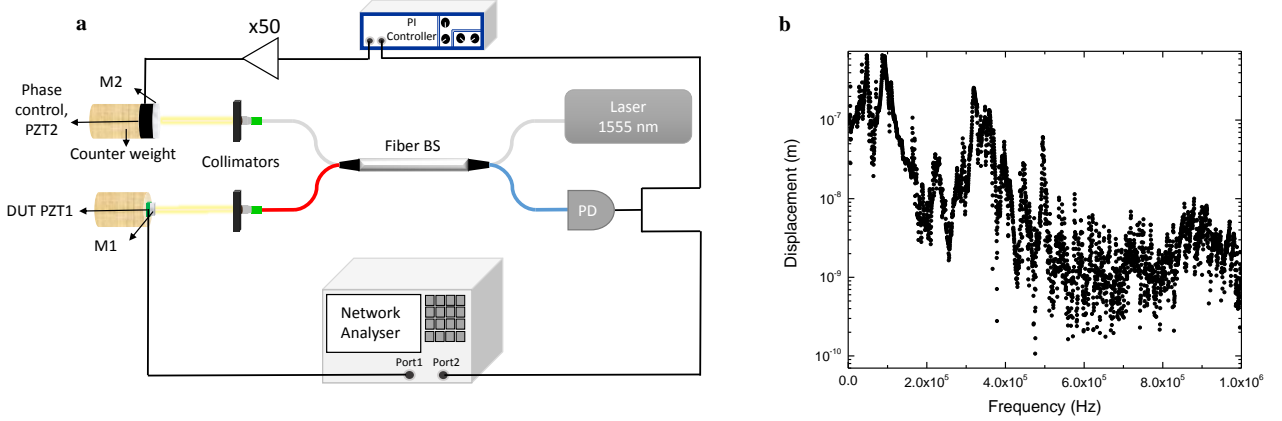


FIG. 3. **Michelson interferometer to calibrate the piezo-electric sound source.** (a) Interferometry measurement scheme. There are two mirrors  $M_1$  and  $M_2$  which are respectively attached to PZT1 and PZT2 which are placed in the output arms of the interferometer. PZT1 is the piezo element to be measured and PZT2 is used to lock the phase of the interferometer. PZT1 and PD are respectively connected to ports 1 and 2 of a NA with which we drive the PZ1 and simultaneously measure the signal of the interferometer. (b) The measured displacement of the PZT1 for a drive voltage of 707 mV at frequency spectrum from 1 kHz to 1MHz.

which was 20 kHz in our measurement.  $V(\omega_{\text{ref}})$  is the photodetector voltage at  $\omega_{\text{ref}}$  and  $V_{\text{max}}$  is the maximum voltage generated by the interference, corresponding to a  $\frac{\lambda}{4}$  displacement. Throughout this measurement we always monitored the generated signal not to saturate i.e., the displacement was always  $< \frac{\lambda}{4}$  at a given applied voltage to the PZT1. We confirmed that the displacement was a linear function of the applied voltage to PZT1. At frequencies where the displacement was larger than  $\frac{\lambda}{4}$ , we lowered the voltage in order to avoid saturation. The high and low voltage measurements were then normalised with respect to 707 mV and compiled. The results are shown in Fig. 3b for an applied voltage of 707 mV.

## VI. FLUIDIC DAMPING OF MICROMECHANICAL DEVICE

In this section we outline expressions and describe an experiment that allow the fluidic damping due to the interaction of our spoked-disk micromechanical resonator with its gaseous environment to be estimated. We follow reference [14]. There are three common forms of fluidic damping relevant to micromechanical devices: ballistic damping, due to

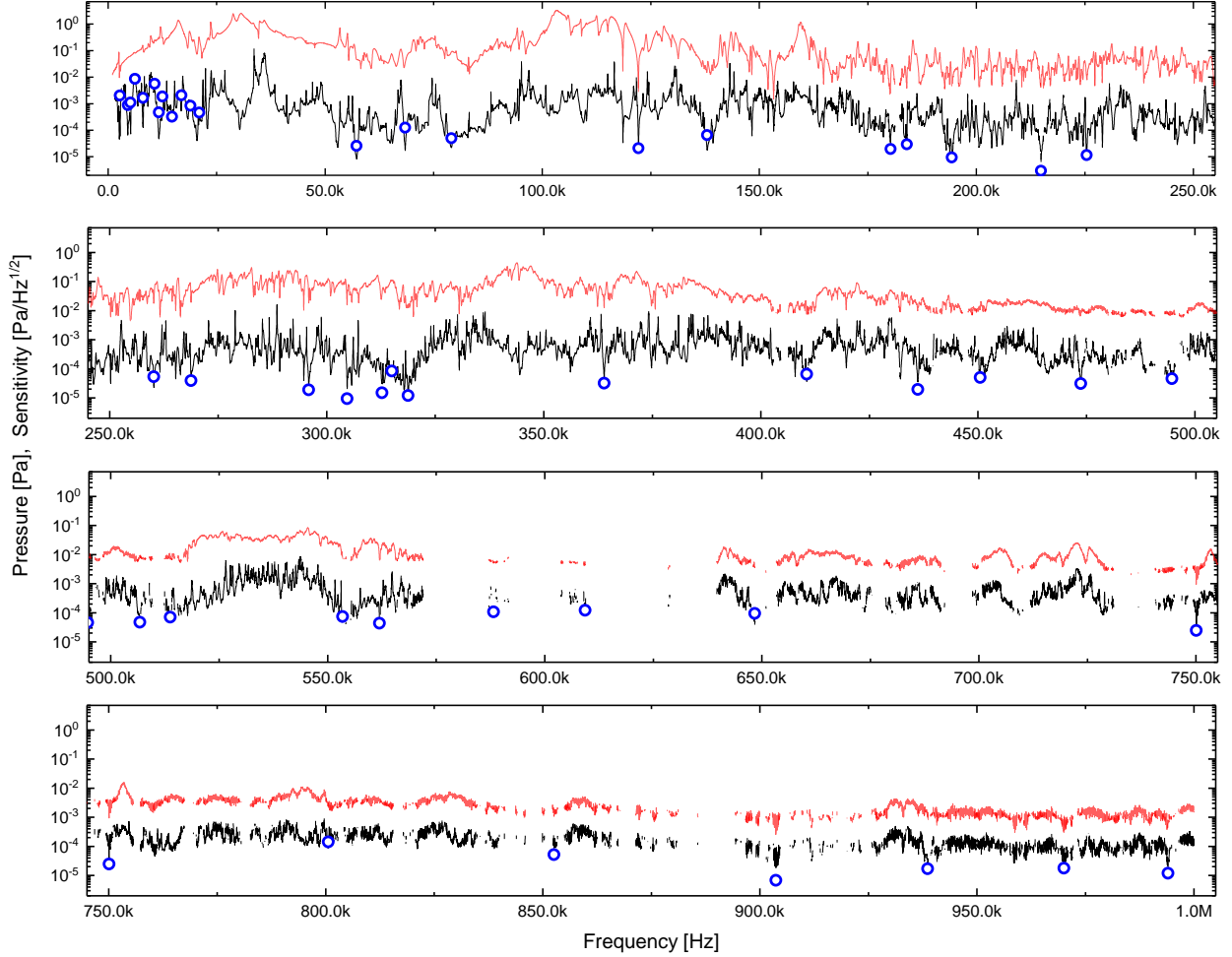


FIG. 4. **Noise equivalent pressure sensitivity.** Pressure sensitivity as a function of frequency (black lines) and the applied pressure (red lines) as measured using a network analyser. The open symbols are reference points directly measured using a spectrum analyser at certain frequencies for further validation of the network analysis.

collisions of gas molecules with the surface of the resonator; drag force damping, due to viscousness of the gas and the velocity gradient between the boundary layer near the surface of the resonator and more distant points in the fluid; and squeeze-film damping, due to the change in pressure introduced by motion of the resonator near its substrate. Ballistic damping is generally only significant in high vacuum conditions, and is therefore not considered further here. The other two forms of damping, in general, introduce a combined force that opposes the velocity of the resonator. Following Chapter 3 in reference [14], and treating the resonator as thin, so that the spatiotemporal eigenmodes  $\mathbf{u}(x, y, z, t)$  which



FIG. 5. **Cross-sectional view of the microfabrication process.** a)-c): Starting from a Oxide-coated Silicon wafer, UV-photolithography and HF-wet-etch were performed to define the Silica structure. d) and e): A  $\text{XeF}_2$  dry-etch isotropically removes silicon and releases the silica-structure.

describe the displacement of each small region of the resonator vary only in the plane of the resonator (defined as the  $\{x, y\}$  plane here), and do not depend on the  $z$ -coordinate (i.e.  $\mathbf{u}(x, y, z, t) = \mathbf{u}(x, y, t)$ ), this force can be written as  $F = -\mu l \dot{\mathbf{u}}(x, y, t)$  where  $\mu$  is the coefficient of viscosity of the fluid and  $l$  is a geometry-dependent characteristic length-scale to be determined later. To find the rate of damping due to the gas  $\gamma_{\text{gas}}$ , this force should be compared to the acceleration of the resonator  $F_{\text{accel}} = m \ddot{\mathbf{u}}(x, y, t)$ , where  $m$  is the effective mass of the mode described by  $\mathbf{u}$ . Considering the acceleration and damping terms in the general equation of motion for harmonic oscillation  $m \ddot{x} + m \gamma \dot{x} + kx = F_{\text{ext}}$ , where  $k$  is the spring constant and  $F_{\text{ext}}$  the external force, we see that  $\gamma_{\text{gas}}$  is given simply by

$$\gamma_{\text{gas}} = \mu l / m \quad (16)$$

in angular units.

The power spectral density of the thermal force noise introduced by fluctuation-dissipation to complement this fluidic dissipation is

$$S_{T,\text{gas}} = 2m\gamma_{\text{gas}}k_B T = 2\mu l k_B T, \quad (17)$$

where, of course,  $k_B$  is the Boltzmann constant, and  $T$  is the temperature of the system. Since the incident acoustic wave travels within the gaseous medium,  $S_{T,\text{gas}}$  presents a fun-

damental bound on the pressure sensitivity of a micromechanical acoustic sensor of fixed geometry and a particular gaseous medium.

Given that the thermal fluctuations introduced by the interaction with the gas are independent from those introduced by thermal vibrations of the substrate and any other damping mechanisms intrinsic to the resonator, the total thermal force noise experienced by the resonator is

$$S_T = 2m(\gamma + \gamma_{\text{gas}})k_B T = 2(m\gamma + \mu l)k_B T, \quad (18)$$

where  $\gamma$  is the intrinsic decay rate of the resonator, and the total mechanical decay rate  $\gamma_m = \gamma + \gamma_{\text{gas}}$ . Inserting this expression into equation (11) we find the minimum detectable pressure

$$P_{\text{min}}(\omega) = \sqrt{S_{\text{PP}}(\omega)} = \frac{1}{rA} \sqrt{2(m\gamma + \mu l)k_B T + N^{-1}|\chi(\omega)|^{-2}}, \quad (19)$$

as given in the main text, where  $r$  is the pressure participation ratio (see main text Fig. 2d), and  $\omega$  is the drive frequency of the acoustic wave. Note that, since the sensor and detection system are linear, the effect on inefficiencies in detection are simply to transform the effective intracavity photon number from  $N \rightarrow \eta N$  where  $\eta$  is the efficiency with which light leaves the optical resonator and is successfully detected at the detector.

### A. Experimental characterisation of the gas damping

In order to determine the contributions to the noise equivalent pressure from intrinsic mechanical dissipation and from fundamental gas damping, we placed the device in a vacuum chamber and swept the pressure from 0.056 mbar to atmosphere. We monitored the damping rate of the resonance observed at 315 kHz. At the lowest measured pressure, the decay rate plateaus to a minimum of 150 Hz, corresponding to the intrinsic mechanical dissipation  $\gamma$ , whereas at atmospheric pressure, the decay rate reaches 1,430 Hz. The difference between these two values corresponds to a gas damping rate of  $\gamma_{\text{gas}} = 1,280$  Hz. Mechanical resonances for three different pressures, measured using a spectrum analyser, are shown in Fig. 6.

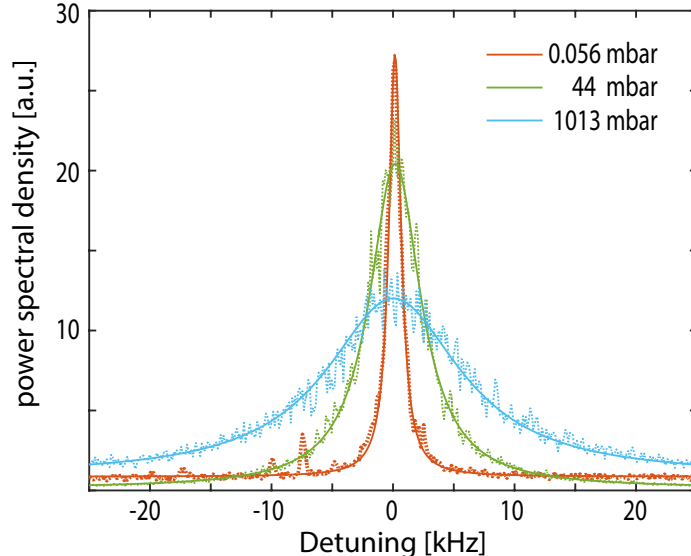


FIG. 6. **Brownian noise spectra of a mechanical resonance with varying static pressure.** Power spectral density versus detuning around the 315 kHz resonance for different pressures with decay rates of 1430 Hz, 535 Hz and 150 Hz at pressures of 1000 mbar, 44 mbar and 0.056 mbar respectively.

### B. Determining the characteristic length-scale

In order to understand the gas damping in our device, we theoretically estimate the expected characteristic viscous length-scale  $l$  for both squeeze film damping and viscous drag damping. As we will see in this subsection,  $l$  is independent of the density and thickness of the resonator, only depending on its mass via its area and height about the substrate. Furthermore, for small device areas,  $l \propto \sqrt{A}$ , decreasing more slowly than the resonator mass as the device size decreases. Consequently, for small and/or low mass resonators, with proper design to minimise the intrinsic damping  $\gamma$  and enhance the optical read-out, it should be possible for the minimum detectable pressure to be limited only by the fundamental gas damping.

Chapter 3 of Ref. [14] gives the drag force for several geometries, with the general form

$$F_{\text{drag}} = -6\pi\xi\mu\sqrt{A}\dot{\mathbf{u}}(x, y, t), \quad (20)$$

where, again,  $\mu$  is the coefficient of viscosity of the fluid, which for air at room temperature is around  $\mu = 1.8 \times 10^{-5}$  kg/m s,  $A$  is the surface area of the top surface of the resonator and  $\xi$  is a dimensionless geometry dependent coefficient which is generally on the order of unity.

For instance, for a free sphere, a vertically moving disk ( $z$  direction), and a horizontally moving disk, it is given by  $\xi = \{1, 0.85, 0.567\}$ , respectively.

Similarly, Ref. [14] calculates the squeeze film force for an annular disk with major and minor radii of  $R$  and  $r$ , respectively, to be

$$F_{\text{squeeze}} = -\frac{3\pi\mu R^4 G(\beta)}{2h^3} \dot{\mathbf{u}}(x, y, t), \quad (21)$$

where  $h$  is the separation of the bottom of the resonator from the substrate,  $\beta = r/R$  and

$$G(\beta) = 1 - \beta^4 + \frac{(1 - \beta^2)^2}{\ln \beta}. \quad (22)$$

Using these expressions, we find directly that

$$l_{\text{drag}} = 6\pi\xi\sqrt{A} = 6\pi^{3/2}\xi\sqrt{R^2 - r^2} \quad (23)$$

$$l_{\text{squeeze}} = \frac{3\pi R^4 G(\beta)}{2h^3}. \quad (24)$$

The total fluidic damping expected for our micromechanical resonator is then given, approximately, by

$$\gamma_{\text{gas}} = \gamma_{\text{drag}} + \gamma_{\text{squeeze}} = \frac{\mu l}{m} = \frac{3\pi\mu}{m} \left( 2\xi\sqrt{A} + \frac{R^4 G(\beta)}{2h^3} \right), \quad (25)$$

while the characteristic length-scale is

$$l = l_{\text{drag}} + l_{\text{squeeze}} = 3\pi \left( 2\xi\sqrt{A} + \frac{R^4 G(\beta)}{2h^3} \right). \quad (26)$$

It is interesting to observe that, since, for a fixed area,  $l$  is independent of the mass of the resonator, as the resonator becomes increasingly thin the gas-damping will eventually dominate damping into the substrate, and for sufficiently good optical measurement, allow the sensor to operate at its fundamental gas-damping force noise floor.

Inserting the relevant parameters of our device of  $\mu = 1.8 \times 10^{-5}$  kg/m s,  $R = 148$   $\mu\text{m}$ ,  $r = 82$   $\mu\text{m}$ ,  $h \sim 33$   $\mu\text{m}$  (an estimate, given the non-flatness of the substrate beneath the device), and a mass of around  $m \sim \rho t A = 252$  ng, where  $\rho = 2650$  kg/m<sup>3</sup> is the density of silica,  $t$  the thickness of the resonator, and  $A$  its area; and choosing  $\xi = 0.75$ , we find

$$\gamma_{\text{drag}}/2\pi \sim 440 \text{ Hz} \quad (27)$$

$$\gamma_{\text{squeeze}}/2\pi \sim 850 \text{ Hz} \quad (28)$$

$$\gamma_{\text{gas}}/2\pi \sim 1,300 \text{ Hz}, \quad (29)$$

where  $\gamma_{\text{gas}} = \gamma_{\text{squeeze}} + \gamma_{\text{drag}}$ .

Similarly we find

$$l_{\text{drag}} \sim 6 \text{ mm} \quad (30)$$

$$l_{\text{squeeze}} \sim 12 \text{ mm} \quad (31)$$

$$l \sim 18 \text{ mm}. \quad (32)$$

Comparing the estimated total gas damping rate  $\gamma_{\text{gas}}$  to the experiment described above, we find good agreement within the uncertainties of the model.

## VII. ESTIMATION OF SENSITIVITY OF TRACE GAS SENSING BY PHOTO-ACOUSTIC SPECTROSCOPY

Photo-acoustic gas spectroscopy is based upon sensing the acoustic waves generated by gas molecules due to the light absorption. Excitation light is properly chosen to be on resonance with one of the spectral lines of the gas molecules. Absorption of light in the gas produces local heating in the sample which results in local pressure increase. If the excitation light is pulsed or a modulated continuous-wave (CW), the generated heat in the gas will result in generation of acoustic waves at the modulation frequency. Photo-acoustic gas sensing is based on measuring the generated acoustic pressure to measure the gas absorption and so the concentration of the sample gas. The optomechanical sensor has high sensitivity together with microscale area. Hence, it offers the possibility to image gas concentrations with high resolution. Here we consider one example, the possibility to measure the  $\text{CO}_2$  exchange of photosynthetic cells.

We can estimate the lowest gas concentration which can be measured by the optomechanical acoustic sensor in vicinity of a photosynthetic sample such as a plant leaf [15]. For this, we need to connect the minimum detectable pressure by the opto-mechanical microphone to the optical absorption coefficient in order to calculate the minimum of gas concentration which can be measured. We consider a microscale photosynthetic sample which exchanges  $\text{CO}_2$  with its environment. We place the acoustic sensor at a distance  $r$  from the sample and shine a pulsed laser through the gas in the vicinity of the sample. We choose the spectral line of  $\text{CO}_2$  at  $\lambda = 4,329.93 \text{ nm}$  ( $k = 2311.105 \text{ cm}^{-1}$ ) having line intensity of  $S = 4.7 \times 10^{-19} \frac{\text{cm}^{-1}}{\text{molec.cm}^{-2}}$ .

For the remainder of the analysis we follow [16] to find the relation between absorption coefficient of the gas and the generated photoacoustic pressure. As in [16], we consider a thin optical medium (low absorption) for which  $\alpha l \ll 1$  where  $\alpha$  is the optical absorption coefficient and  $l$  is irradiation length or length of the photoacoustic source. We further assume that the sound wave can exit the irradiated zone within the pulse duration so that  $R_s < v\tau_L$ , where  $R_s$  is the radius of the laser beam,  $v$  is the speed of sound and  $\tau_L$  is the laser pulse duration. Therefore, the effective source radius is  $R = v\tau_L$ . The second assumption can therefore be rewritten as  $R_s < R$ , i.e. that the radius of the laser beam should be smaller than the source radius. Moreover, the source volume can be written as  $V = \pi R^2 l$ . The coefficient of expansion of air,  $\beta$  is

$$\beta = \frac{\Delta V}{V \Delta T}, \quad (33)$$

where  $\Delta V = \pi(R + \Delta R)^2 l$  is the initial expansion of the source volume after the laser beam, and  $\Delta T$ , the rise in the temperature after a pulse, is [16]

$$\Delta T = \frac{E \alpha l}{\rho V C_p}, \quad (34)$$

in which  $E$  is the energy of the laser pulse,  $\rho$  is the density and  $C_p$  is the heat capacity of air. Therefore,  $\Delta R$ , the initial expansion of the source radius becomes [16]

$$\Delta R = \frac{\beta E \alpha}{2\pi \rho C_p v \tau_L}. \quad (35)$$

The peak displacement,  $U_s(r)$  at distance  $r$  from the photoacoustic source varies as  $\frac{1}{r}$  for spherical sound waves. Hence,

$$U_s(r) = \Delta R \left( \frac{R}{r} \right) = \frac{\beta E \alpha}{2\pi \rho C_p r}. \quad (36)$$

the peak acoustic pressure is [16]

$$P_{\text{peak}}(r) \approx \frac{v \rho U_s(r)}{\tau_L}. \quad (37)$$

Equations (36) and (37) result in

$$\alpha \approx \frac{2\pi C_p \tau_L r}{v \beta E} P_{\text{peak}}(r). \quad (38)$$

To calculate the minimum detectable concentration we first need to relate the peak acoustic pressure to the effective acoustic pressure driving the mechanical mode over a period of the

mechanical motion. The conversion factor can be estimated as the ratio of the laser pulse duration and the mechanical period over which the pressure is being applied. We have

$$P_{\text{eff}}(r) = P_{\text{peak}}(r)\tau_L\frac{\omega_m}{2\pi}, \quad (39)$$

in which  $\omega_m$  is the mechanical frequency. Moreover, the absorption coefficient is proportional to gas concentration as

$$\alpha = \frac{cS}{2\gamma_G}, \quad (40)$$

in which  $S = 4.7 \times 10^{-19} \frac{\text{cm}^{-1}}{\text{molec.cm}^{-2}}$  is line intensity of CO<sub>2</sub>,  $\gamma_G = 0.06 \text{ cm}^{-1}$  is gas linewidth of and  $c$  is the number density of gas molecules. Using equations (38), (39) and (40) we can write

$$c_{\text{min}} \approx \frac{8\pi^2\gamma_G C_p r}{v\beta E S \omega_m} P_{\text{eff-min}}, \quad (41)$$

where  $P_{\text{eff-min}}$  is the minimum pressure that can be detected by the optomechanical transducer and  $c_{\text{min}}$  is the minimum detectable gas molecules number density. At room temperature,  $T = 300 \text{ K}$ ,  $\beta = 0.0034 \frac{1}{\text{K}}$  and  $C_p = 1.005 \frac{\text{kJ}}{\text{kg.K}}$ . We further assume a pulsed laser having a pulse energy of  $E = 1 \mu\text{J}$  and a pulse duration of  $\tau_L = 1 \mu\text{s}$ . This pulse duration is short enough to satisfy the condition of  $R_s < v\tau_L$  for a typical laser beam radius of  $R_s = 50 \mu\text{m}$  but also long enough to avoid thermal diffusion during the exposure. If we choose the acoustic frequency of  $\nu_0 = 318 \text{ kHz}$  at which the optomechanical sensor can detect acoustic pressures as small as  $P_{\text{min}} = 12 \mu\text{Pa}$ , using equation (41) at  $r = 100 \mu\text{m}$ , we get  $c_{\text{min}} = 5.3 \times 10^{10} \frac{\text{molec}}{\text{cm}^3}$  which is equal to 1.8 ppb. The concentration of CO<sub>2</sub> around leaf cells investigated in [15] is of the order of 100 ppm. Therefore, our sensor can be expected to be sensitive enough to measure CO<sub>2</sub> exchange of photosynthetic cells with a high resolution.

## VIII. MEASUREMENT OF THE ACOUSTIC WAVES GENERATED BY THE NANOSCALE VIBRATIONS OF CELLS OR BACTERIA

Bio-identifications are required in various fields including medicine, food and beverages, water, safety, public health and security. Current procedures of bacteria detection are costly, time-consuming and based on cell culture which require laboratory and microscopic analysis done by a trained person. However, self-contained mobile bio-sensors can simplify fast diagnosis in place even for the some bacteria that can not be cultured in laboratory [17].

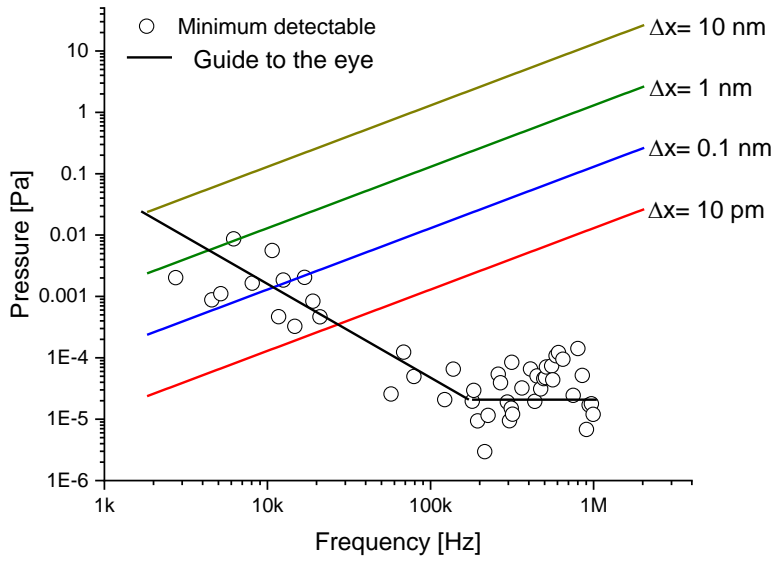


FIG. 7. **Opto-mechanical acoustic sensor performance for cell vibration detection.** The circles are experimental sensitivities (at a bandwidth of 1 Hz) for our sensor with given size. Our sensor is scalable and it can be fabricated slightly larger or smaller thereby changing its sensitivity at different frequency. However, more or less the solid black line shows a guide to the eye for expected sensitivity of such sensor we have. The color solid lines show the amount of pressure generated by the cell versus frequency for different displacements.

There are recent experiments on bacteria, yeast and plant cell samples in liquid and soil which show bacteria and yeast produce vibrations with displacement amplitudes of 1-100 nm and plant cells produce vibrations with displacement amplitude of 1-30 nm [18–21]. These experiments are performed for cell concentrations of  $10^8$  and  $10^7$  CFU/ml which respectively include 96 and 27 bacteria per sample [20]. This is a quite good sensitivity in bio-sensing. Our opto-mechanical acoustic sensor can be used to study micro-organisms through detecting these vibrations and hence there is no need to grow cells in an especial probing medium. We can consider a very thin layer of bacteria or cell in a liquid which is coated on a silicon or glass substrate and hold our acoustic sensor very close to the sample such that we can ignore the air attenuation of the acoustic waves generated by cells. In order to estimate if our sensor is sensitive enough to probe such vibrations, we need to estimate the pressure produced by these micro-organisms vibrations and compare it with the minimum pressure that our sensor can detect at a given frequency. The pressure generated

by the vibrational displacements can be calculated as

$$P = \pi\nu_0 Z_{\text{air}} d, \quad (42)$$

in which  $\nu_0$  is the vibration frequency,  $Z_{\text{air}} = 413 \text{ Pa}\cdot\text{s}/\text{m}$  is air impedance and  $d$  is the displacement. For  $\nu_0 = 10 \text{ kHz}$  and  $d = 1 \text{ nm}$  we have  $P = 1.3 \times 10^{-2} \text{ Pa}$  which suggests that our acoustic sensor can detect cell vibrations. Fig. 7 shows how the opto-mechanical sensor performs for cells vibrating at other frequencies and with smaller displacement amplitudes. As can be seen, the sensor is able to resolve signals from biological entities and of course the higher the frequency the smaller the minimum detectable displacement of parts of the cell.

Our opto-mechanical acoustic sensor can also offer some other advantages for cell detection such as using this sensor one does not need an agent as in [18–21] since the sensor can measure cells vibration without need to attach them to the sensor. Moreover, we can detect the magnitude and frequency of the vibrations and scan over xy coordinates to map the vibrational pattern. This enables studying and investigating different bacteria in a sample. This sensing enables the experimenter to measure spectral density of the acoustic waves generated by the cell which may help to understand the difference between different types of cells (maybe cancer detection) or many other cell biology investigation such as probing fast phenomena happening on the cell wall or inside it. The cell wall can also behave like a membrane transferring internal oscillations to the air and finally to the sensor. This suggest that our sensor has significant potential in developing micromechanical sensors for micro-organisms.

- 
- [1] Henriquez, T. A. An ExtendedRange Hydrophone for Measuring Ocean Noise. *J. Acoust. Soc. Am.*, **52**, 1450-1455 (1972).
- [2] Hillenbrand, J., & Sessler, G. M. High-sensitivity piezoelectric microphones based on stacked cellular polymer films (L). *J. Acoust. Soc. Am.*, **116**, 3267-3270 (2004).
- [3] Hsu, P-C., C. H. Mastrangelo, & K. D. Wise. A high sensitivity polysilicon diaphragm condenser microphone. *Micro Electro Mechanical Systems, 1998. MEMS 98. Proceedings., The Eleventh Annual International Workshop on. IEEE*, 580-585 (1998).
- [4] <http://www.acopacific.com/chart.html>
- [5] Bucaro, J. A., Lagakos, N., Houston, B. H., Jarzynski, J., & Zalalutdinov, M. Miniature, High performance, low-cost fiber optic microphone. *J. Acoust. Soc. Am.*, **118**, 1406-1413 (2005).
- [6] Jo, W., Kilic, O., & Digonnet, M. J. Highly sensitive phase-front-modulation fiber acoustic sensor. *J. Light. Technol.*, **33**, 4377-4383 (2015).
- [7] Bucaro, J. A., Dardy, H. D., & Carome, E. F. Fiberoptic hydrophone. *J. Acoust. Soc. Am.*, **62**, 1302-1304 (1977).
- [8] Akkaya, O. C., Akkaya, O., Digonnet, M. J., Kino, G. S., & Solgaard, O. Modeling and demonstration of thermally stable high-sensitivity reproducible acoustic sensors. *J. Microelectromech. Syst.* **21**, 1347-1356 (2012).
- [9] Ma, Jun, et al. Fiber-optic FabryPerot acoustic sensor with multilayer graphene diaphragm. *IEEE Photon. Technol. Lett.* **25**, 932-935 (2013).
- [10] Preisser, Stefan, et al. All-optical highly sensitive akinetic sensor for ultrasound detection and photoacoustic imaging. *Biomed. Opt. Express*, **7**, 4171-4186 (2016).
- [11] Gardiner, C. & Zoller, P. *Quantum Noise: A Handbook of Markovian and Non-Markovian Quantum Stochastic Methods With Applications to Quantum Optics* (Springer Science & Business Media, 2004).
- [12] Walls, D.F. & Milburn, G.J. *Quantum Optics* (Springer Science & Business Media, 2007).
- [13] Bowen, W.P. & Milburn, G.J. *Quantum Optomechanics* (CRC Press, 2015).
- [14] Bao, M. *Analysis and design principles of MEMS devices* (Elsevier, 2005).
- [15] Ho, Q. T., Verboven, P., Yin, X., Struik, P. C., & Nicolai, B. M. A microscale model for combined CO<sub>2</sub> diffusion and photosynthesis in leaves. *PloS One*, **7**, e48376 (2012).

- [16] Tam, A. C. Applications of photoacoustic sensing techniques. *Rev. Mod. Phys.* **58**, 381 (1986).
- [17] Ahmed, A. et al. Biosensors for whole-cell bacterial detection. *Clin. Microbiol. Rev.* **27**, 631-646 (2014).
- [18] Longo, G. Rapid detection of bacterial resistance to antibiotics using AFM cantilevers as nanomechanical sensors. *Nat. Nanotechnol.* **8**, 522 (2013).
- [19] Kasas, S. et al. Detecting nanoscale vibrations as signature of life. *Proc. Natl. Acad. Sci. U.S.A.* **112**, 378-381 (2015).
- [20] Lissandrello, C. et al. Nanomechanical motion of Escherichia coli adhered to a surface. *Appl. Phys. Lett.* **105**, 113701 (2014).
- [21] Song, L. et al. Nanoscopic vibrations of bacteria with different cell-wall properties adhering to surfaces under flow and static conditions. *ACS nano*, **8**, 8457-8467 (2014).